The Dependence of the Fraction of Active Galactic Nuclei in Groups and Clusters on Host Galaxy Morphology

A Senior Honors Thesis

Presented in Partial Fulfillment of the Requirements for graduation *with research distinction* in Astronomy in the undergraduate colleges of The Ohio State University

by

Timothy Arnold

The Ohio State University
December 2008

Project Adviser: Professor Paul Martini, Department of Astronomy

ABSTRACT

Comparison of the incidence and properties of Active Galactic Nuclei (AGN) in the field, groups, and clusters of galaxies can provide new information about how AGN are triggered and fueled, similar to how galaxy environment has been used to study the processes that drive galaxy evolution. As the morphological mix of galaxies varies substantially with environment, and there is evidence that the AGN fraction depends on morphological type, we present the first study of the incidence of AGN as a function of galaxy morphology in 11 groups and 5 clusters of galaxies to disentangle the effects of environment and morphology on the AGN fraction. Specifically, we have performed a quantitative morphological analysis of galaxies more luminous than $M_R = -20$ mag and compared X-ray identified AGN with inactive galaxies. Our analysis suggests that the AGN fraction is higher in groups of galaxies relative to clusters for both early-type and late-type galaxies, and that therefore the previously observed increase in the AGN fraction in groups of galaxies is not solely due to the larger fraction of more gas-rich, late-type galaxies in lower-velocity dispersion groups.

1. Introduction

The physical mechanisms that trigger and fuel low-luminosity Active Galactic Nuclei (AGN) are not well understood. For luminous, distant quasars, major mergers are considered the dominant mechanism for AGN triggering and fueling. Studies indicate that a large fraction of these galaxies are morphologically disturbed, with nearby neighbors, tidal tails, multiple nuclei, or linked by luminous matter to other nearby galaxies (Gehrens, Fried, Wehinger, & Wyckoff 1984; Hutchings, Crampton, Campbell 1984; Malkan, Margon, & Chanan 1984; Smith et al. 1986). These results have motivated the hypothesis that lower luminosity AGN in the nearby Universe are, like quasars, activated and fueled by galaxy interactions or mergers. However, for these nearby AGN, there is as yet no evidence to support the claim that mergers are the source of their fuel. If gas-rich mergers or interactions are the primary mechanism for activating and fueling nearby AGN, one expects higher AGN fractions in environments where galaxies have an abundant supply of gas and where there exist large number densities of galaxies, leading to high interaction probabilities. The cluster environment has, by definition, very high number densities, but galaxies in the centers of rich clusters have proportionally less cold gas than those in less dense environments (e.g. Giovanelli & Haynes 1985). Galaxies in the field have abundant supplies of cold gas from the intergalactic medium, but the relatively small number densities in this environment (and thus available nearby neighbors with which to interact) might preclude AGN triggering or fueling. An intermediate group environment may offer the ideal circumstances for the triggering and fueling of low luminosity AGN

in the nearby Universe. A comparison of the incidence and properties of AGN in different number density environments, with consideration paid to host galaxy morphology, can provide new information about these AGN.

The forms and shapes of galaxies were studied even before they were known to be extragalactic objects, and since then numerous physical properties have been tied to galaxy morphology. Most galaxies can be decomposed into a bulge and disk component. This aids in morphological modeling and is justifiable as a physical description. The extremes of this model exist as elliptical galaxies, which contain only a bulge or spheroid component, and pure disk galaxies, which lack a bulge component. Most other galaxies fall somewhere in between, representable by a combination of disk and bulge components. It has also been shown that the growth of the bulge of a galaxy seems to be tied to that of the supermassive black hole (SMBH) at its center. Ferrarese & Merritt (2000) and Gebhardt et al. (2000) discovered a relationship between SMBH mass and stellar velocity dispersions in the bulge of a galaxy. Since AGN are a consequence of matter accreting on to a central SMBH, and the relation between SMBH mass and stellar velocity dispersion implies that the SMBH influences the evolution of the host galaxy bulge, it is reasonable to suppose that a relationship might exist between galaxy morphology—and specifically the mass of the bulge of spheroid—and AGN properties. Galaxy morphology also traces other observable properties of galaxies. Elliptical galaxies and early-type disk galaxies, which have a significant bulge component, tend to be redder and lack active star formation, while disk-dominated galaxies are bluer and are often undergoing active star formation. Additionally, it has been shown that galaxy morphology, and thus often physical properties, vary greatly with local galaxy density. Dressler (1980) showed that the abundance of early-type galaxies increases with increasing galaxy density and that of late-type, disk-dominated systems. This correlation persists over many orders of magnitude and extends smoothly, from clusters, through groups, and into the lowest density field environment. This environmental dependence of galaxy morphology has motivated many investigations of the physical mechanisms responsible for the changes in morphology that are presumably the result of neighboring galaxies. The list of mechanisms that may affect morphology is extensive and includes: mergers, ram-pressure stripping via interaction with the intra-cluster medium (ICM) (Gunn & Gott 1972; Quilis, Moore, & Bower 2000), evaporation by the hot ICM (Cowie & Songaila 1977), and starvation of new gas that would otherwise replenish the interstellar medium (Larson et al. 1980; Balogh et al. 2000).

Though morphology has been used extensively to analyze galaxy evolution, for much of this time galaxy morphology was ascertained by eye. This process, though largely repeatable, lacks quantitative robustness and is a protracted process for large numbers of objects. The alternative—determining morphology in an automated fashion—is not simple to implement. Only in the last decade, with the development of large-format, linear detectors and substantial computational resources, has it become commonplace to classify galaxies using quantitative and repeatable tech-

niques. Datasets consisting of large numbers of galaxies have made visual inspection impractical as a method for determining morphology (there have, however, been novel approaches at morphological identification via visual inspection; see Lintott et al. (2008)), and abundant computational resources have made quantitative analyses more practical. Various methods to ascertain morphology quantitatively exist in the literature (Conselice, Bershady, & Jangren 2000; Goto et al. 2003; Haeussler et al. 2007), and we choose to use the galaxy fitting code GALFIT (Peng et al. 2002) to obtain morphological properties for galaxies in our sample.

Motivated by the fact that black hole growth is linked to bulge evolution (Ferrarese & Merritt 2000; Gebhardt et al. 2000), and that AGN are understood to be the result of matter accreting on a central SMBH (Lynden-Bell 1969), one expects a relationship between galaxy morphology and AGN incidence and activity. In fact, it has been suggested that AGN actively alter the course of galaxy evolution (Begelman 2004), e.g. by quenching star formation in quasars (Di Matteo, Springel, & Hernquist 2005; Hopkins, et al. 2005; Springel, Di Matteo, & Hernquist 2005). Observations of nearby galaxies also show that the incidence of AGN is a function of galaxy morphology (Ho et al. 1997; Kauffmann et al. 2003). Since AGN activity is related to the host galaxy morphology, and galaxy morphology is a function of environment, a correlation between AGN fraction and environment can be explained in two ways: (1) directly by the environment itself or (2) indirectly by the change in morphological mix with environment. The aim of the present study is to determine which of these explanations is correct, or if both are important. Many studies analyzing the AGN fraction across varying galaxy environments that have focused exclusively on a particular morphological type (thus removing the bias from the morphology-density relationship) have found that the AGN fraction may be constant across varying environments (Shimada et al. 2000; Miller et al. 2003; Kauffmann et al. 2004; Grogin et al. 2005), though these studies do not include X-ray identified AGN or galaxies in rich clusters. In the densest environments, spectroscopic studies have shown that the AGN fraction drops by a factor of 5 relative to the field (Dressler et al. 1985) but given the different galaxy morphology distributions, it is not clear whether the variation in AGN fraction among different environemnts is due solely to the diverse morphological mixes or whether there are properties inherent to a particular environment that affect the incidence of AGN.

The typical way AGN are identified in surveys is via properties of their optical spectra. Line flux ratios (or equivalent width ratios) are used to distinguish AGN from galaxies undergoing active star formation (Baldwin, Phillips, & Terlevich 1981; Kewley et al. 2001; Kauffmann et al. 2004). Alternatively, and only more recently, X-ray luminosities, X-ray spectral properties, and X-ray to optical flux ratios have been used to detect the presence of AGN. Furthermore, X-ray techniques are more sensitive to lower luminosity AGN than optical spectra for nearly all cases, particularly when the spectra have low signal to noise. Early X-ray instruments had insufficient resolution to separate AGN and X-ray emission from the ICM for most clusters, but with the advent of more advanced instruments like *Chandra* and *XMM-Newton*, surveys have found many AGN in

the cluster environment (e.g. Martini et al. 2006). X-ray sources have been analyzed whose X-ray luminosities and spectral shapes suggest AGN are the source of the X-ray radiation (rather than low mass X-ray binaries, hot X-ray luminous gas, or star formation; see Sivakoff et al. (2008)). Using these new instruments, the AGN fraction among luminous cluster galaxies (M_R < -20) was found by Martini et al. (2006) to be 5% in eight low-redshift clusters, dramatically higher than the 1% AGN fraction found via optical selection by previous studies (Dressler et al. 1985). This surprising confirmation of a large number of AGN in cluster centers partly motivated this study into the morphological properties of these X-ray AGN and the inactive population of other members in the cluster.

In this paper, we analyze 5 nearby clusters and 11 groups of galaxies to discover possible relationships between quantitative morphological parameters and X-ray AGN demographics. We are motivated to extend our morphological and X-ray AGN analysis to groups as environments with high number density but low velocity dispersion are ideal to analyze the possible effects of galaxy interactions. In addition, approximately 55% of all galaxies in the local Universe are located in groups (Eke et al. 2004). We find that the X-ray AGN fraction is a property that is not exclusivley determined by galaxy morphology—that the observed increase in AGN fraction in groups relative to clusters is not a sole consequence of the larger fraction of gas-rich, late-type galaxies in the group environment.

The X-ray observations and the optical images to obtain morphological fits are described in § 2, we describe our methods regarding morphological analysis in § 3, we present our findings in § 4, discuss these results in § 5, and make concluding remarks in § 6.

2. Observations and Sample Selection

For all of the galaxies in our sample, we obtained visible-wavelength images to perform the morphological analysis and used X-ray data to determine if a galaxy hosted an AGN. The visible wavelength images were obtained from two sources: the Sloan Digital Sky Survey (SDSS) and the Las Campanas Observatory in Chile. X-ray data were acquired from the *XMM-Newton* satellite and the *Chandra X-ray Observatory*. We removed galaxies from our sample which fell outside of the field of view for the respective X-ray observations and those that were less luminous than $M_R = -20$. In three of the clusters, the available optical images did not include all of the galaxies in the X-ray field of view. For the remaining groups and clusters, morphological information for all confirmed group or cluster members were obtained. Table 1 contains information about the groups and clusters in our sample.

We obtained data from five low-redshift clusters of galaxies ($0.05 < z < 0.07$) originally pre-

sented and analyzed in Martini et al. (2006), Martini et al. (2007), and Sivakoff et al. (2008). The galaxies were chosen as they were located in a field of view for which publicly available *Chandra* ACIS data were available with sufficient exposure times to detect objects at our X-ray luminosity limit at the cluster redshift. Many of these clusters had data from visible-wavelength observations acquired with the 2.5m du Pont telescope at Las Campanas Observatory with either the Wide Field Reimaging CCD (WFCCD) or Tek5 CCD cameras. For the galaxies that did not, clusters Abell 85 and Abell 89B, we obtained publicly available optical data from the SDSS Data Release 6 (Adelman-McCarthy et al. 2008).

Optical data from SDSS DR6 were obtained for eleven groups of galaxies ($0.02 < z < 0.06$) from the XI (XMM/IMACS) Groups Project, which contains groups from the Merchán & Zandivarez (2002) catalog. These groups were chosen for the existence of X-ray data from *XMM-Newton* in the same field of view as optical images available from the SDSS. More information about the selection of these groups and the X-ray observations can be found in Mulchaey et al. (2009).

3. Morphological Analysis

Our primary goal was to analyze the morphology of our galaxy samples in a robust and reliable way and determine how host galaxy morphology is related to the AGN fraction in our group and cluster samples. We opted to use GALFIT, an extensible two-dimensional fitting algorithm developed by Peng et al. (2002), although note that other algorithms and codes that recover galaxy morphology exist in the literature (Conselice, Bershady, & Jangren 2000; Simard 2002; Goto et al. 2003). One motivation for our choice of GALFIT comes from Haeussler et al. (2007), who compared GALFIT to GIM2D (Simard 2002), another fitting code, and concluded that GALFIT has advantages in its ability to simultaneously fit neighbors in a crowded field and benefits from a dramatic increase in execution speed.

GALFIT is designed to extract structural components from galaxies by fitting two-dimensional light profiles with an arbitrary number of parametric functions that are suitable for describing the surface brightness distribution of galaxies. Although designed to fit subtle structures of well resolved galaxies with many-component models simultaneously, it is also effective at handling large numbers of galaxies imaged at lower resolution, fitting their surface brightness profiles with relatively simple models. We utilize the latter capability in our analysis. GALFIT takes as input a simple text file and is very customizable, allowing easy extension via a wrapping script. Finally, GALFIT can use a variety of analytic functions singly or simultaneously, including the Sérsic profile.

3.1. Models

The Sérsic (1968) profile is a generalization of the popular de Vaucouleur's $r^{1/4}$ profile, developed first to fit galactic bulges and elliptical galaxies by de Vaucouleurs (1948). The Sérsic profile is defined in the following way:

$$\Sigma(r) = \Sigma_e \exp\left[-\kappa\left(\left(\frac{r}{r_e}\right)^{1/n} - 1\right)\right], \quad (1)$$

where Σ_e is the surface brightness (flux per unit area) at the effective radius r_e, defined such that half of the total flux is within r_e. κ is coupled to the other free parameters to ensure this condition to be true (Peng et al. 2002). The most useful parameter is the Sérsic index, n. The shape of the light profile depends strongly on this parameter, such that the bulge-like de Vaucouleurs profile corresponds to a Sérsic index of $n = 4$ and an exponential light profile characteristic of disk galaxies corresponds to $n = 1$. A combination of de Vaucouleurs bulge and exponential disk can be used to decompose many galaxies into their bulge and disk components and many regular galaxies can be described with such a bulge and disk composition.

We have chosen to use two methods to quantify galaxy morphology. First, we use the versatile Sérsic profile, with n varying continuously, describing all galaxies from predominantly disk like systems to bulge dominated ellipticals. This method has been used in the literature extensively to classify galaxies as early-type or not, often using $n = 2.5$ as a point to distinguish between early- and late type morphologies (with $n > 2.5$ associated with early-type galaxies). Studies using data from the SDSS have determined a cutoff near $n = 2.5$, and others have shown that $n = 2.5$ was a reliable point of demarcation to distinguish early-type from late type morphologies (e.g. Bell et al. (2004a); also see McIntosh et al. (2005) and references therein). We will follow these precedents and also use $n = 2.5$ as a point to distinguish between early- and late-type galaxies. Second, we perform a two component bulge-to-total flux decomposition by fitting the galaxy with a de Vaucouleurs bulge (a Sérsic profile with $n = 4$) simultaneously with an exponential disk ($n = 1$). The ratio of the flux contribution from the bulge component with the total flux contribution is calculated, and this too is a measure of galaxy morphology. We primarily will use the Sérsic index as a measure of morphology, but also present the bulge-to-total flux decomposition as evidence of the effectiveness of our morphological fits.

Finally, when available, we compared our calculated morphological parameters to the SDSS `fracdev` parameter, which is a quantity calculated by the SDSS pipeline and serves as a quantitative measure of galaxy morphology. `fracdev` is very similar to our bulge-to-total flux decomposition. It is obtained by fitting the surface brightness profile of a galaxy with exponential and de Vaucouleurs components, and then keeping the fractional contribution of the latter. Bernardi et al. (2005) considered `fracdev` > 0.8 to unambiguously identify an early-type morphology.

3.2. GALFIT

GALFIT accepts as input a plain text file that specifies the initial conditions for models and other options and parameters related to the fit. GALFIT can accomodate as many fits as the user desires, limited only by computational capabilities. Thus, one can use several simple models to represent various components of a well resolved and structurally complex galaxy, or one could alternatively use a single, simple model for a less resolved galaxy. It is also possible to fit adjacent or blended objects in addition to the object of interest (hereafter target), removing potential contamination, in order to obtain a more robust fit of the target. GALFIT convolves the model with a point spread function (PSF) supplied by the user, subtracts the convolved model from the input image, and computes the reduced chi squared, χ^2_ν :

$$\chi^2_\nu = \frac{1}{N_{\rm dof}} \sum_{x=1}^{nx} \sum_{y=1}^{ny} \frac{\left(\mathrm{flux}_{x,y} - \mathrm{model}_{x,y}\right)^2}{\sigma^2_{x,y}}, \tag{2}$$

where $N_{\rm dof}$ is the number of degrees of freedom in the model, flux & model are the pixel values of the original image and analytic model, respectively, and $\sigma^2_{x,y}$ is the error in each pixel. GALFIT minimizes χ^2_ν using a Levenberg-Marquardt algorithm, a downhill-gradient type algorithm suited for searching large parameter spaces quickly. Additional and optional input includes a pixel weight map (values of $\sigma_{x,y}$ at each point), although if this is not supplied, one is generated from the image itself and the image header values for the gain and read-noise), a bad pixel map specifying which pixels should be excluded from the χ^2_ν calculation (i.e. masked out), and initial guesses for the many free parameters, including object position and morphological quantities. GALFIT is useful in its extensibility, and we took advantage of this by creating a wrapper script to fit large numbers of objects with little to no user interaction.

3.3. Measurement

We have created an algorithm that utilizes GALFIT to analyze large numbers of objects of interest and accurately obtain their relevant morphological parameters. The script performs autonomously with positive results that prove comparable to a human user fine tuning parameters until an ideal fit is obtained.

Our input is a list of astrometric coordinates of objects of interest and the possible FITS images with these objects. We calculate whether or not the object lies within the image boundaries and obtain initial morphological parameters (e.g. a measure of the galaxy's radius, magnitude, ellipticity, object position, and position angle) to be used as the initial inputs to the GALFIT minimization routine. We collect these initial morphological parameters by extracting the sources from

the image using the tool SExtractor (Bertin & Arnouts 1996). For each image, GALFIT requires a PSF. These were created manually, approximating them with a Gaussian generated by the IRAF routines `imcreate`, `imreplace`, and `gauss`. Effective radii of the Gaussian PSFs were approximated by examining several stars in the image using IRAF. We also determined that small variations in the radius of the PSF negligibly affected the parameters of the model, confirming the robustness of this method of PSF creation.

When we determine the initial parameters of targets from SExtractor, we also collect this information for all detected objects within some arbitrary number of effective radii from the target. The fitting region supplied to GALFIT is determined in a similar way. Based on the various parameters of the objects in the field of view, we either add the pixels associated with the object to the bad pixel file, masking them out and removing them from the χ^2_ν calculation and fitting procedure, or fit the object in addition to the target object. This discriminatory algorithm compares object brightness to the target brightness (e.g. a very dim object will likely be masked out rather than fit) and the distance from the target (e.g. an object very distant from the target will likely be masked out rather than fit). In this way we only fit additional objects if they are likely to contaminate the fit of our target, and thus its morphological properties. Fitting a superfluous number of objects is computationally wasteful and complicates finding a unique minimum in χ^2_ν space.

We then generate a GALFIT input file for both a single component Sérsic profile fit and a two component Sérsic profile & Exponential Disk fit, the latter used for a bulge-to-total flux ratio calculation. Several iterations of this dual method fitting occur if the resultant χ^2_ν values for each method differ by more than a small fraction, with the previous fit parameters used for subsequent iterations, to achieve confidence that the solution obtained is not the result of the algorithm getting lost in a local minimum. This propensity to get lost in a local minimum and the question of a multi-component solution's uniqueness in large parameters spaces is an issue for algorithms such as GALFIT, and Peng et al. (2002) addresses this question in depth (see their § 3.3).

Our output includes screenshots of the input image, the model image generated by the GALFIT and convolved with the image PSF, and the residual image (the difference of the data and the model images). These three images are saved as a single image for each fit technique (single and two-fit methods) for quick visual inspection. We also retain the fit log files generated by GALFIT, FITS images that contain the actual models generated by the algorithm, and append a text file with the relevant morphological parameters and object information for later analysis. The script that automates these tasks is written in Python and works for for an arbitrarily large set of input targets without the need for user intervention.

3.4. Fit Examples

In Figure 1 we show several examples of the images that are produced by this algorithm. The panels were chosen to be representative of the different environments studied and of the different quality and type of the images. We also display examples of the relative merits and weaknesses of our method. Further descriptions of some of the panels are found in the following paragraphs, and morphological properties as obtained from our methods for these examples can be found in Table 2.

Figure 1, Panel E shows a galaxy in a nearby cluster, A644, where many objects have been removed by subtraction. Only one object was fit with GALFIT—the target object—and all the others are sufficiently far or dim enough so that they do not interfere with the fitting procedure. To obtain a low value of χ^2_ν , the pixels from these other objects in the field of view were simply masked out.

Figure 1, Panel H depicts a similar problem which is solved with the other method mentioned. Here, rather than a field contaminated with moderately but not overwhelmingly bright objects far from the target, we encounter a situation in which the target is blended with a nearby object. Multiple objects are fit with GALFIT in this situation in order to extract the morphological properties that would otherwise be obscured by blending. In addition, the objects that are far from the target are still masked out as in the previous figure, to obtain the best value of χ^2_ν . Two other examples of this phenomenon can be seen in Panels A & B.

Figure 1, Panels D & F show how we used two different methods and fitting strategies in order to gain more morphological information about the objects we are interested in. Panel D depicts the object fit by a Sérsic profile, and Panel F depicts the same object fit by a de Vaucouleurs bulge plus exponential disk profile. We can further be assured that we have reached a unique solution to fitting these objects by checking to see that the values obtained by the independent methods of fitting arrive at a similar value of χ^2_ν . Typically, if both fits are successful, this is the case.

Figure 1, Panel G shows an example of our simple models proving inadequate for a galaxy with more subtle morphological features (see § 3.5). This galaxy sufficiently deviates from an "ideal" single or double-component model and is resolved well enough that this is problematic. It also seems that the target could be blended with other objects to the extent that SExtractor is unable to separate them from the target.

Finally, Panel C shows the results for a galaxy from the $z \approx 0.05$ group RXCJ1002.6+3241, where optical images were obtained from the SDSS.

Table 1. Clusters and Groups

Cluster/Group	Right Ascension	Declination	Redshift	σ_v [km s^{-1}]	N^*_{gal}	Data Sources
A85	00:41:50.4	-09:18:11	0.0554	993 (+85) (-85)	109	(1),(3)
A89B	00:42:54.6	-09:13:50	0.0770	474 (+155) (-155)	22	(1),(3)
A3125	03:27:17.9	-53:29:37	0.0616	475 (+94) (-94)	20	(2),(3)
A3128	03:30:43.8	-52:31:30	0.0595	906 (+74) (-74)	67	(2),(3)
A644	08:17:25.6	-07:30:45	0.0701	952 (+382) (-382)	19	(2),(3)
RXCJ0110.0+1358	01:10:05.5	+13:58:49	0.0581	745 (+74) (-64)	24	(1),(4)
RXCJ0746.6+3100	07:46:37.3	+31:00:49	0.0579	719 (+97) (-59)	20	(1),(4)
RXCJ0844.9+4258	08:44:56.7	+42:58:54	0.0550	343 (+75) (-34)	11	(1),(4)
RXCJ1002.6+3241	10:02:38.6	+32:41:58	0.0505	454 (+58) (-39)	22	(1),(4)
RXCJ1022.0+3830	10:22:04.7	+38:30:43	0.0544	710 (+77) (-54)	31	(1),(4)
RXCJ1122.2+6712	11:22:14.5	+67:12:46	0.0553	223 (+27) (-23)	15	(1),(4)
RXCJ1204.4+0154	12:04:25.6	+01:54:04	0.0203	495 (+59) (-45)	9	(1),(4)
RXCJ1223.1+1037	12:23:06.5	+10:37:26	0.0255	334 (+51) (-32)	3	(1),(4)
RXCJ1324.1+1358	13:24:11.9	+13:58:45	0.0233	303 (+47) (-29)	6	(1),(4)
RXCJ1440.6+0328	14:40:38.2	+03:28:25	0.0269	449 (+41) (-30)	12	(1),(4)
RXCJ1604.9+2355	16:04:57.0	+23:55:14	0.0321	423 (+58) (-36)	6	(1),(4)

Note. — (1): SDSS DR6 Photometry, Adelman-McCarthy et al. (2008) (2): 2.5m du Pont Telescope, Martini et al. (2006), (3): *Chandra X-ray Observatory*, Martini et al. (2006); Sivakoff et al. (2008), (4): *XMM-Newton*. *Number of confirmed members.

Table 2. Example Fit Properties from Figure 1

Panel Letter	Cluster/Group	Object Name	Sérsic Index	χ^2_ν	Bulge-to-Total Flux Ratio	χ^2_ν
A	A85	J004112.22-091010.3	3.40	1.565	0.956	1.564
B	A3128	J033037.72-523257.7	1.88	1.280	0.518	1.269
C	RXCJ1002.6+3241	J100303.61+323652.7	2.25	1.453	0.765	1.441
D	RXCJ0844.9+4258	J084444.24+425953.2	4.17	1.540	0.931	1.540
E	A644	J081718.97-072835.9	1.90	5.554	0.589	5.207
F	RXCJ0844.9+4258	J084444.24+425953.2	4.17	1.540	0.931	1.540
G	RXCJ1223.1+1037	NGC4320 (J122257.80+103255.0)	3.96	2.313	0.977	2.316
H	A3125	J032724.78-532517.6	3.28	1.642	1.000	1.676

Note. — Illustrative GALFIT decompositions of select galaxies in the groups and clusters studied in this paper.

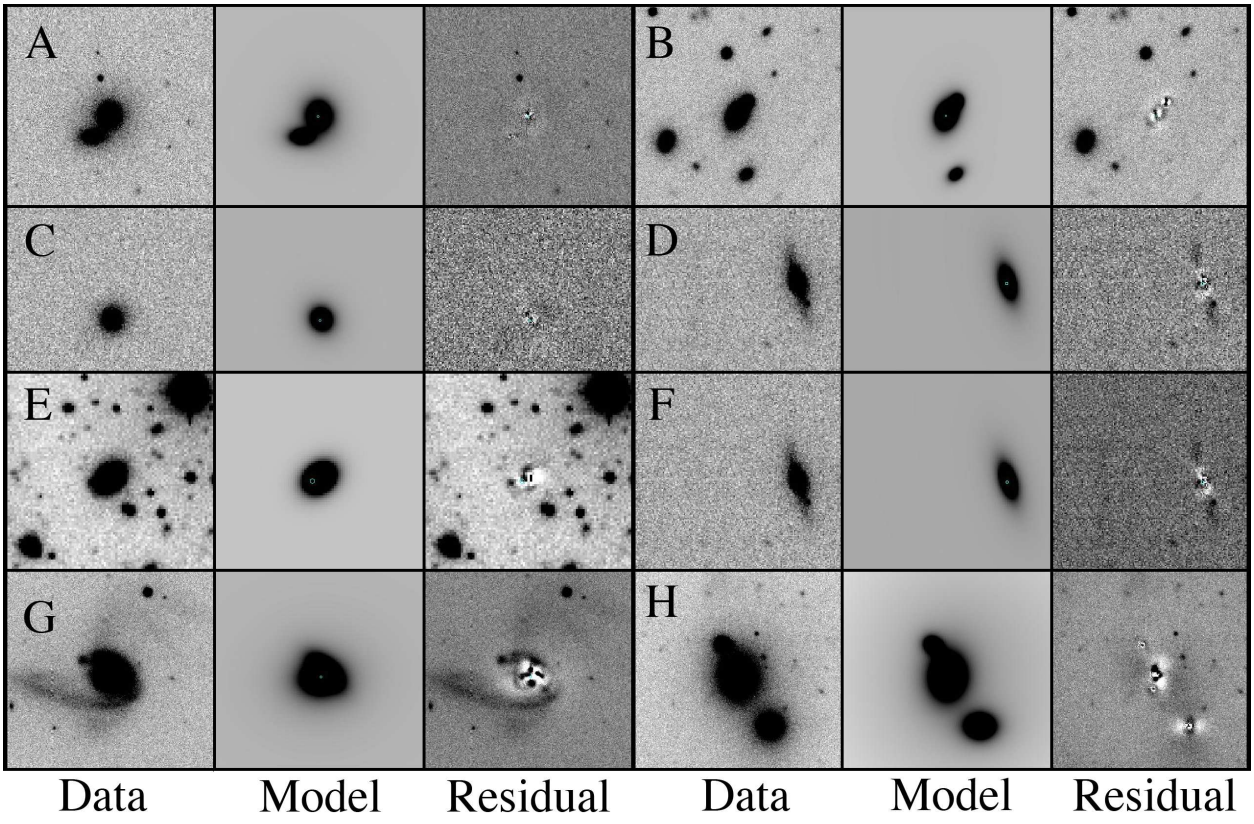

Fig. 1.— Illustrative GALFIT decompositions of select galaxies in the groups and clusters studied in this paper. For morphological parameters acquired in the fitting process, see Table 2.

3.5. Fit Problems

As the algorithm used by GALFIT is optimized for speed and is searching a very large parameter space, the probability of getting lost in a local minimum is nonnegligible. Though we cannot be certain that this has not happened, we employ several techniques to guard against this possibility. As mentioned above, we run the GALFIT minimization algorithm on each object several times and update the initial fit parameters if the resultant χ^2_ν differs by more than several percent between the two different fitting methods. Additionally, as described in § 3 we have employed two different numbers to quantify the galaxy morphology: the Sérsic index in the single component fit and the bulge-to-total flux ratio in the two component fit. We expect these quantities to be highly correlated (see Figure 2) and we reexamine egregious outliers from such a plot. Finally, we save images of the initial object, model, and residual as a single image. These files can be inspected by eye, quickly discovering fits that are failures for various reasons.

Stubborn objects that are not fit well by our procedure persist, though they are relatively few. As described in § 3, GALFIT was created by Peng et al. (2002) to have the ability to decompose the complex structure of well resolved galaxies. We, instead, use it to do simple single or, at most, two-model fits. For our typical resolution, this is not a problem. However, some of our images of galaxies are so well resolved that a simple Sérsic profile or de Vaucouleurs bulge plus exponential disk fit is insufficient to adequately describe the available data. Structures such as bars or strong spiral arms are sometimes fit rather than the more averaged picture of the galaxy that would be obtained with a less-resolved image of the object. Also, we occasionally find objects that are blended with the target and cannot feasibly be fit away with GALFIT. This is a problem particularly if SExtractor fails to find the blended object as a separate source.

3.6. Checks on Success

We used various methods to quantify morphology in order to verify the effectiveness of our methods: the Sérsic index, the bulge to total flux ratio, and, in some cases, SDSS `fracdev`. We compare these different quantities graphically, in Figures 2 & 3. Figure 2 shows the relationship between the two morphological parameters that we used, Sérsic index and bulge-to-total flux ratio. We did not fit a line to this relationship, as the scatter in the points is considerably more significant than in the `fracdev` relationship, but nominally we can see that a bulge to total flux ratio of about 0.6 is associated with a Sérsic index of 2.5. This number, as expected, is consistent with the value obtained by a similar comparison with SDSS `fracdev`.

Figure 3 shows the relationship between Sérsic index *n* and SDSS `fracdev` for our group sample that was taken from SDSS, and thus has these data for analysis. The parameter `fracdev`

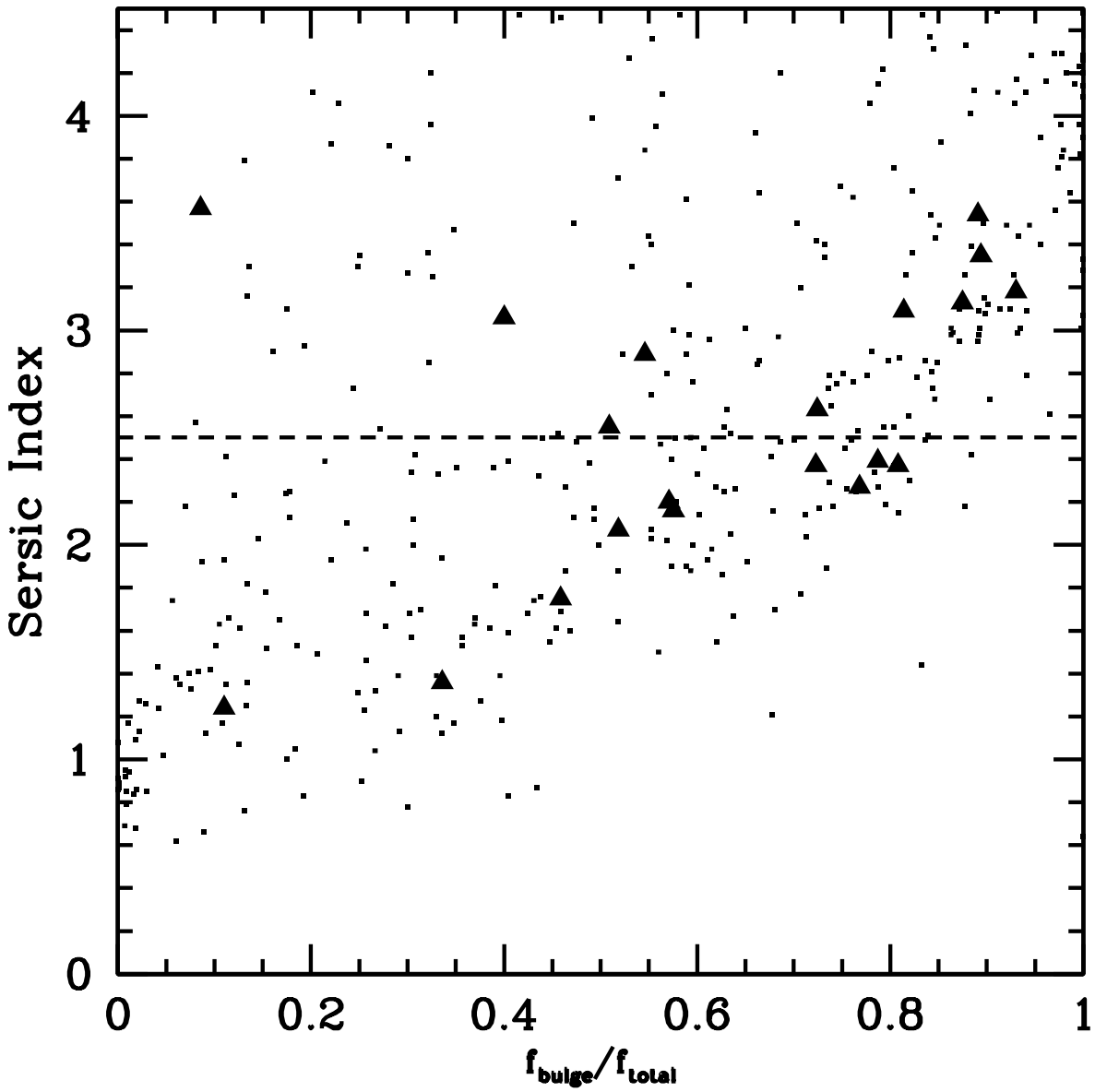

Fig. 2.— Bulge to total flux ratio versus Sérsic index for all of the groups and clusters in our sample. Triangles indicate AGN and squares indicate inactive galaxies. This plot includes all the galaxies successfully fit with GALFIT. The dotted line indicates $n = 2.5$.

seems to saturate for extremely bulge-dominated systems (note the abundance of points lying at `fracdev` = 1 for increasing values of n); for this reason, we have excluded these saturated points from the linear fit shown. The resulting fit gives a value of `fracdev` = 0.66 associated with $n = 2.5$, roughly consistent with the value (> 0.8, Bernardi et al. (2005)) in the literature for early-type demarcation.

While we cannot guarantee the uniqueness of the GALFIT solutions, analyzing these graphs and checking other results throughout the process provides assurances. We (1) visually inspect resultant fits and residuals, (2) Examine not only the absolute value of χ^2_ν for each fit, but check to see if the value of χ^2_ν for the two different fitting methods are consistent with one another, and (3) inspect figures like Figures 2 & 3 and identify outliers for possible refitting or other reanalysis.

4. AGN Fractions

For the galaxies in the our sample, we performed the analysis described in § 3. We then compiled information regarding the morphology of the groups we studied, shown in Table 3. The second part of our analysis entails relating the galaxy morphologies with the incidence of AGN in the samples. One way to identify AGN as distinct from star forming galaxies is by examining line flux ratios such as [OIII]λ5007/Hβ and [NII]λ6584/Hα . The location of the galaxies in question on a BPT diagram (Baldwin, Phillips, & Terlevich 1981) allows one to classify the galaxy as an AGN or a galaxy undergoing star formation. Typically, if the line flux ratios satisfy a certain criterion, (e.g. Equation 1 in Kauffmann et al. (2003)) they can be identified as AGN. Alternatively, galaxies can be identified due to properties in their X-ray emission. This latter method is what we have used to identify AGN and is described in detail in, e.g., Sivakoff et al. (2008). This AGN identification is required to calculate AGN fractions, and AGN fractions with respect to a particular morphological type relies on AGN identification in addition to morphological classification as obtained by our methods described in § 3.

In Table 3, we show the morphological results of our analysis. In this table, we see the number of objects fit from the sample. This typically includes all of the objects in the sample, but in some cases the total number of objects in the group or cluster are not all fit. This occurs when optical images do not exist in our observations for particular objects, or, more rarely, if our procedure produces an unusable fit or no fit at all. Column 3 is the number of objects fit in the sample with an early-type morphology, or a galaxy for which the Sérsic index for its single-component fit is $n > 2.5$. Column 4 is the fraction of galaxies in the group that are early-type as determined by the Sérsic index. The error bars are calculated as single-sided, one sigma confidence intervals (Gehrels 1986). Columns 5 & 6 are the total number of objects in the sample, confirmed and estimated, if applicable. Column 7 is the number of objects in the entire sample with an early-

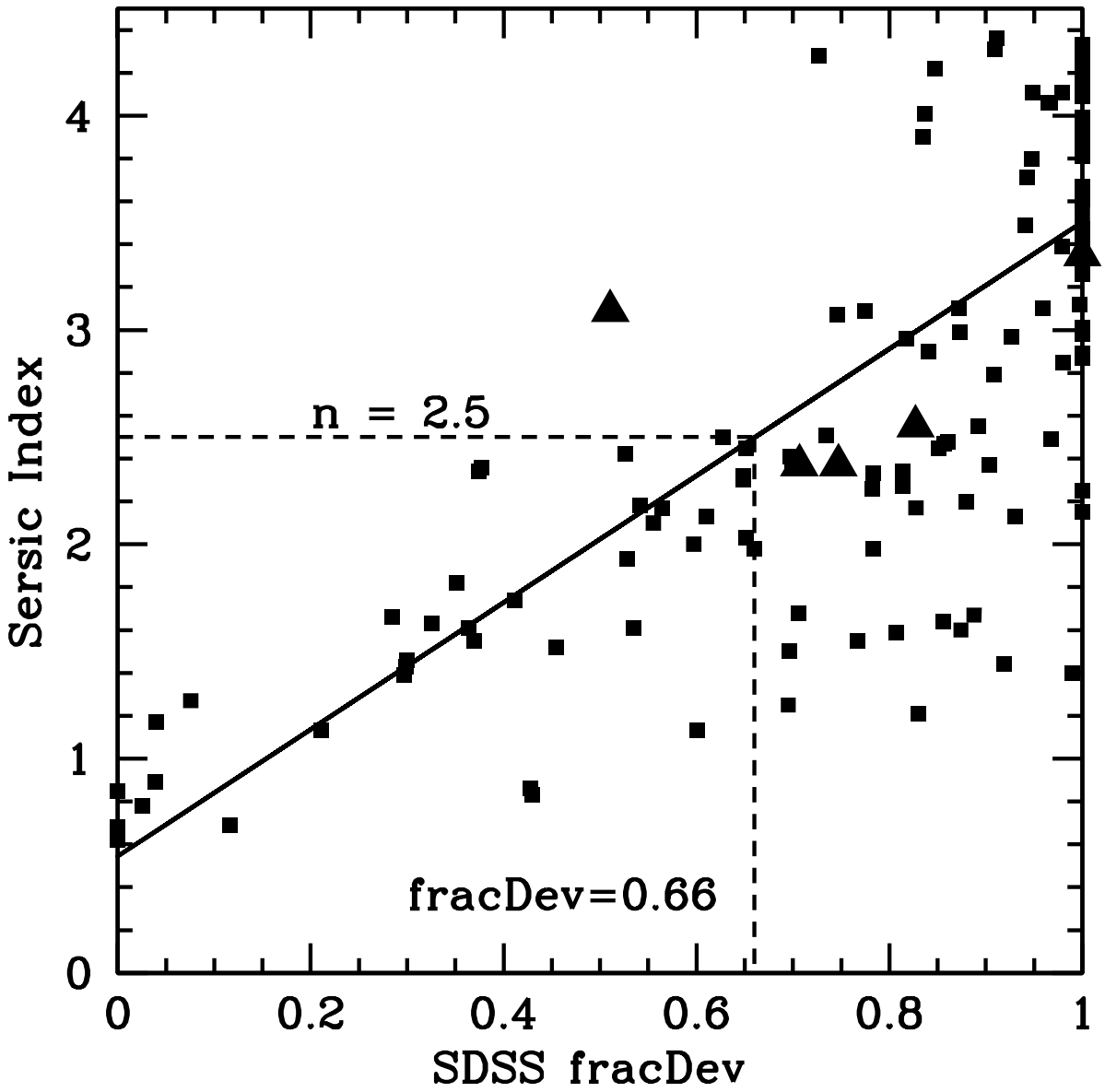

Fig. 3.— Sérsic index versus SDSS `fracdev` parameter. Triangles indicate AGN and squares indicate inactive galaxies. This plot only includes our subsample with SDSS images (and thus having associated `fracdev` values) only. See Table 1. The dotted lines indicate $n = 2.5$ and the interception of the fit line with $n = 2.5$, at `fracdev` = 0.66.

Table 3. Morphological Results

Cluster / Group	$N_{\rm fit}$	$N_{{\rm fit},n>2.5}$	$f_{n>2.5}$	— $N_{\rm total}$ —		$N_{{\rm total},n>2.5}$
(1)	(2)	(3)	(4)	(5)	(6)	(7)
A85	109	79	$0.725^{+0.114}_{-0.112}$	109	109	79
A89B	22	10	$0.455^{+0.216}_{-0.185}$	22	22	10
A3125	18	10	$0.556^{+0.270}_{-0.238}$	20	28	16
A3128	54	21	$0.389^{+0.117}_{-0.104}$	67	67	26
A644	15	7	$0.467^{+0.278}_{-0.231}$	19	75	35
RXCJ0110.0+1358	24	17	$0.708^{+0.217}_{-0.170}$	24	24	17
RXCJ0746.6+3100	20	16	$0.800^{+0.254}_{-0.198}$	20	20	16
RXCJ0844.9+4258	11	8	$0.727^{+0.359}_{-0.252}$	11	11	8
RXCJ1002.6+3241	22	12	$0.545^{+0.207}_{-0.155}$	22	22	12
RXCJ1022.0+3830	31	9	$0.290^{+0.133}_{-0.095}$	31	31	9
RXCJ1122.2+6712	15	7	$0.467^{+0.251}_{-0.172}$	15	15	7
RXCJ1204.4+0154	9	7	$0.778^{+0.419}_{-0.287}$	9	9	7
RXCJ1223.1+1037	3	2	$0.667^{+0.879}_{-0.431}$	3	3	2
RXCJ1324.1+1358	6	2	$0.333^{+0.440}_{-0.215}$	6	6	2
RXCJ1440.6+0328	12	6	$0.500^{+0.299}_{-0.198}$	12	12	6
RXCJ1604.9+2355	6	5	$0.833^{+0.564}_{-0.360}$	6	6	5

Note. — Morphological and demographic information for our three samples. (1) Cluster or group name. (2) Number of objects fit in our analysis by GALFIT. (3) The number of those objects that has a Sérsic index $n > 2.5$. (4) Fraction of objects fit with Sérsic index $n > 2.5$. (5) Total number of objects in the sample (confirmed). (6) Total number of objects in the sample (estimated). (7) Total number of objects in the sample with $n > 2.5$ (inferred if estimated population differs from confirmed; actual if otherwise).

type morphology, either directly from Column 3 or inferred from the early-type fraction and the estimated membership total. These numbers (Columns 6 & 7) rarely differ from Columns 2& 3.

Table 4 gives details about the number of X-ray identified AGN in each group or cluster, as well as the AGN fraction and early-type X-ray fraction. Details about the X-ray AGN selection criteria and the AGN candidacy of galaxies are obtained from Martini et al. (2006) and Sivakoff et al. (2008). Martini et al. (2006) performed X-ray analyses of the galaxies and determined whether or not they were likely AGN candidates based on their X-ray spectral shapes and multi-wavelength flux ratios, and describe the process in detail in § 2.1 of that paper. Sivakoff et al. (2008) made some minor revisions to AGN candidacy status in some of the clusters from the Martini et al. (2006) study; we adopt those modifications here. Sivakoff et al. (2008) also added X-ray AGN candidacy information for two of the clusters we analyze that were absent in Martini et al. (2006). The first column of this table is the name of the group or cluster; Column 2 is the number of X-ray identified AGN fit in our sample with an early-type morphology; Column 3 is the number of fit objects of any morphology identified as X-ray AGN. Column 4 gives the fraction of X-ray AGN in the cluster, calculated as the number of X-ray AGN divided by the number of total members in the cluster (the latter is given in Table 3).

Due to the small number of AGN in our group samples, it is difficult to draw conclusions about relations between quantities like the AGN fraction of the individual groups and the velocity dispersion—a proxy we use for number density—of a group. Rather, our discussion of the AGN fraction in the groups will be centered on analyzing and understanding AGN fractions for an amalgamated sample of galaxies, binned according to velocity dispersions. These fractions will contain more AGN, reducing the size of the error bars.

4.1. General X-ray AGN Fraction

The AGN fractions for each group and cluster are calculated and displayed in Table 4. The AGN fraction for each group and cluster is calculated by dividing the number of X-ray galaxies included in the sample (Column 3 in Table 4) by the total number of galaxies in the sample (Column 6 in Table 3). This fraction is the value obtained in Column 4 of Table 4. The error bars are derived from Poisson statistics and are single-sided, one sigma confidence intervals. Some of the X-ray AGN fractions are zero, and in this case the same error calculation is used to provide an upper limit (see many of the groups in Table 4).

Figure 4 plots the X-ray AGN fraction versus velocity dispersion. The figure shows all of the groups or clusters with nonzero X-ray fractions (those with only upper limits are excluded for clarity, though they are included in the calculation of the binned fractions as described below).

Squares indicate groups with velocity dispersion of less than 500 km s^{-1}; triangles indicate clusters with a velocity dispersion of greater than 500 km s^{-1}. There is a suggestive but inconclusive trend towards smaller AGN fractions with increasing velocity dispersion. This suspicion is confirmed when we bin the data by velocity dispersion. In the right panel of Figure 4, the X-ray fraction of all of the clusters with velocity dispersions greater than 500 km s^{-1} and groups with a velocity dispersion of less than 500 km s^{-1} have been averaged and plotted. The error bars, like those of the individual groups and clusters on the graph, are single-sided, one sigma confidence intervals. Following the procedures in Sivakoff et al. (2008) and Gehrels (1986), we find that the probability that the error bars overlap is small (0.8%). However, as there are 120 ways in which we could combine the groups and clusters (and we chose the most significant), we cannot unequivocally make a claim that the two populations are distinct from one another. We observe only a suggestive trend.

4.2. Early-type X-ray AGN Fraction

To investigate if the difference between groups and clusters is driven by the change in morphological mix, we now compute the X-ray AGN fraction for early-type galaxies alone. The early-type X-ray AGN fraction for each group and cluster is calculated by dividing the number of X-ray galaxies that are of an early-type morphology (Sérsic index greater than 2.5, Column 2 in Table 4) by the total number of galaxies in the sample that are of an early-type morphology (Column 7 in Table 3). This fraction is the value obtained in Column 5 of Table 4. The error bars are derived in the same way as in the general AGN fraction (§ 4.1).

Figure 5 plots the early-type X-ray AGN fraction versus velocity dispersion. Like Figure 4, this figure shows all of the groups or clusters with nonzero early-type X-ray fractions (those with only upper limits are again excluded for clarity). Figures 4 & 5 are quite similar: one observes the same suggestive but inconclusive trend towards smaller early-type AGN fractions with increasing velocity dispersion. We again bin the groups and clusters, as in Sivakoff et al. (2008). In the right panel of Figure 5, the X-ray fraction of all of the clusters with velocity dispersions greater than 500 km s^{-1} and the groups with velocity dispersions of less than 500 km s^{-1} have been averaged and plotted. The error bars, like those of the individual groups and clusters on the graph, are single-sided, one sigma confidence intervals. Following the procedures in Sivakoff et al. (2008) and Gehrels (1986), we find a small probability that the error bars overlap (0.9%). However, as again there are 120 ways in which we could combine the groups and clusters (and we chose the most significant), we cannot make a strong claim that the populations are distinct from one another. Instead, the data are suggestive of a correlation. Figure 5 contains additional information compared to Figure 4, however. We have plotted a value from the literature for the early-type X-ray AGN

Table 4. X-ray AGN Fractions

Cluster/Group (1)	$N_{X,fit,n>2.5}$ (2)	$N_{X,fit}$ (3)	f_X (4)	$f_{X,n>2.5}$ (5)
A85	2	2	$0.018^{+0.024}_{-0.012}$	$0.025^{+0.033}_{-0.016}$
A89B	2	2	$0.091^{+0.120}_{-0.059}$	$0.200^{+0.264}_{-0.129}$
A3125	2	3	$0.107^{+0.106}_{-0.063}$	$0.125^{+0.168}_{-0.090}$
A3128	3	4	$0.060^{+0.048}_{-0.030}$	$0.115^{+0.114}_{-0.068}$
A644	1	2	$0.027^{+0.035}_{-0.018}$	$0.029^{+0.066}_{-0.024}$
RXCJ0110.0+1358	0	0	$0.000^{+0.077}_{-0.000}$	$0.000^{+0.108}_{-0.000}$
RXCJ0746.6+3100	1	1	$0.050^{+0.115}_{-0.041}$	$0.062^{+0.144}_{-0.052}$
RXCJ0844.9+4258	1	1	$0.091^{+0.209}_{-0.075}$	$0.125^{+0.287}_{-0.103}$
RXCJ1002.6+3241	0	0	$0.000^{+0.084}_{-0.000}$	$0.000^{+0.153}_{-0.000}$
RXCJ1022.0+3830	1	2	$0.065^{+0.085}_{-0.042}$	$0.111^{+0.255}_{-0.092}$
RXCJ1122.2+6712	3	3	$0.200^{+0.195}_{-0.109}$	$0.429^{+0.417}_{-0.233}$
RXCJ1204.4+0154	0	0	$0.000^{+0.205}_{-0.000}$	$0.000^{+0.263}_{-0.000}$
RXCJ1223.1+1037	0	0	$0.000^{+0.614}_{-0.000}$	$0.000^{+0.920}_{-0.000}$
RXCJ1324.1+1358	1	1	$0.167^{+0.383}_{-0.138}$	$0.500^{+0.500}_{-0.414}$
RXCJ1440.6+0328	0	1	$0.083^{+0.192}_{-0.069}$	$0.000^{+0.307}_{-0.000}$
RXCJ1604.9+2355	0	0	$0.000^{+0.307}_{-0.000}$	$0.000^{+0.368}_{-0.000}$

Note. — X-ray AGN demographics and fractions for the cluster and group samples. (1) Cluster / group name. (2) Number of X-ray identified AGN fit in our sample with early-type morphology ($n > 2.5$). (3) Number of all X-ray identified AGN fit in our sample. (4) Fraction of fit galaxies that are X-ray identified AGN. (5) Fraction of fit galaxies that are X-ray AGN and have early-type morphologies ($n > 2.5$).

fraction as found by B. Lehmer (2006, private communication, see Martini et al. (2007)) (6.6%) for comparison. Intriguingly, the group and cluster early-type AGN fractions are consistent with the field value.

5. Discussion

The results of our analysis as presented in Figures 4 & 5 have the potential to teach us about AGN triggering, fueling, and galaxy evolution, but ultimately fall short of offering a compelling conclusion. It has been suggested in the literature that the AGN fraction decreases with increasing number density and thus velocity dispersion (e.g. Dressler et al. (1985)). It has also been suggested that the AGN fraction is constant across a wide range of number density environments (Shimada et al. 2000; Miller et al. 2003; Kauffmann et al. 2004; Grogin et al. 2005). These studies, however, all focused on a different detection method than this study. Focusing on X-ray AGN should yield a different result than the traditional optical spectroscopic detection methods, as suggested by Martini et al. (2006). Thus, the weak trend observed in Figure 4 would not be surprising. The values of the X-ray AGN fraction as calculated from our methods among only increases in every group or cluster (except one, and it is difficult to say for those with only an upper limit) when moving from the general X-ray AGN fraction to the specific early-type X-ray AGN fraction. This growth of the fraction seems to happen in every number density environment we probed, apparent from the nearly identical probabilities with which we calculate exclusivity based on our binning procedure (most conservatively, 36% probability that the two X-ray AGN fractions are distinct, and 33% probability that the two early-type X-ray AGN fractions are distinct from one another).

If our weakly observed trend of decreasing X-ray AGN fraction is real, and additionally, if that trend exists in the early-type X-ray fraction, we can conclude that even when isolating a particular morphological type, we observe a decrease in X-ray AGN fraction in high number density environments. That is, this would suggest that the observation of a paucity of AGN in more dense environments is not solely a consequence of the different morphological mix, but is in fact related to a fundamental property of that galaxy environment. Perhaps these overdense environments sufficiently strip galaxies of available fuel for AGN activity, despite the large number of neighbors with which galaxies can interact. We note that the field early-type X-ray AGN fraction (B. Lehmer 2006, private communication) suggests that the fraction again falls for field galaxies. This could be caused by a lack of neighbors to trigger AGN despite an abundance of available gas for fuel. The group environment could be the ideal environment—with an abundance of fuel because there are not enough neighboring galaxies to deplete it but still enough neighbors for possible interaction—for the triggering and fueling of low-luminosity nearby X-ray AGN. In this scenario, the cluster environment is too dense, the field environment too sparse, and the environment in which most

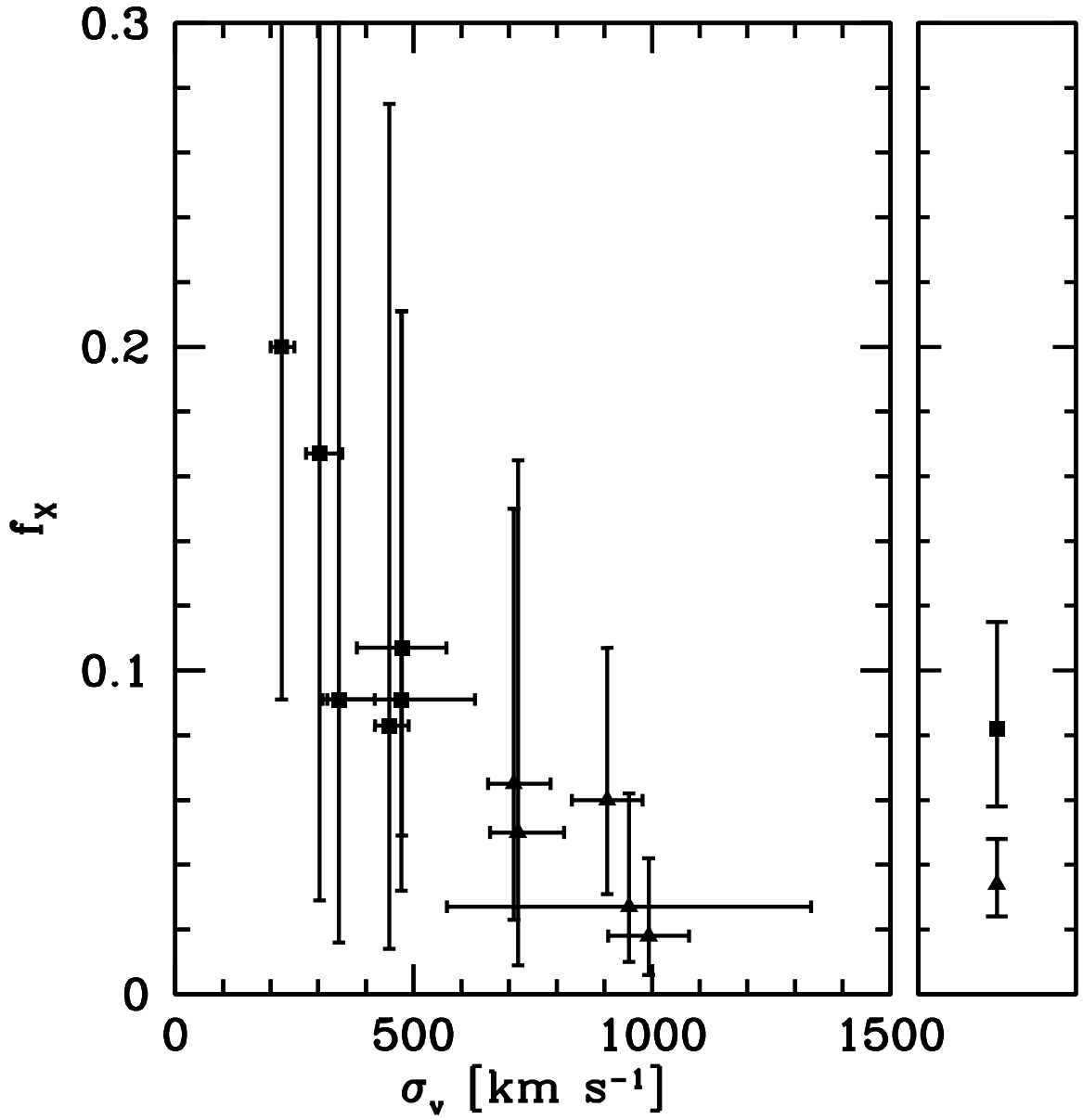

Fig. 4.— X-ray AGN fraction versus velocity dispersion. The points indicate groups or clusters with $\sigma < 500$ km s^{-1} (*squares*) and groups or clusters with $\sigma > 500$ km s^{-1} (*triangles*). Following Sivakoff et al. (2008), the right panel shows the average AGN fraction for $\sigma < 500$ km s^{-1} (*square*), $\sigma > 500$ km s^{-1} (*circle*).

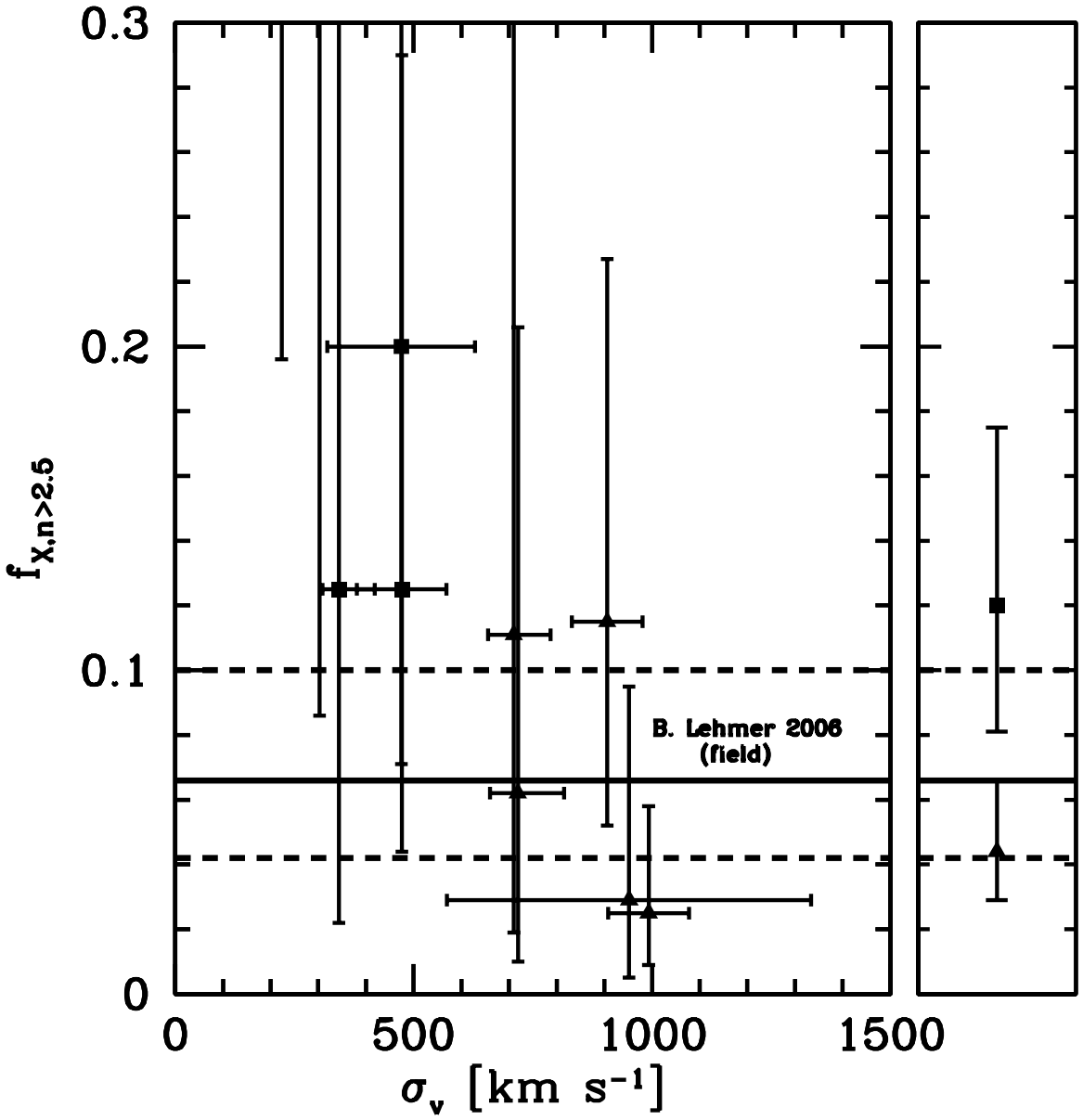

Fig. 5.— Early type X-ray AGN fraction versus velocity dispersion. The points indicate groups or clusters with $\sigma < 500$ km s^{-1} (*squares*) and groups or clusters with $\sigma > 500$ km s^{-1} (*triangles*). Following Sivakoff et al. (2008), the right panel shows the average AGN fraction for $\sigma < 500$ km s^{-1} (*square*), $\sigma > 500$ km s^{-1} (*circle*).

galaxies exist—the group—is just right for AGN triggering and fueling.

6. Summary

We have conducted the first quantitative morphological analysis of the AGN fraction in dense environments with a sample of 5 clusters and 11 groups. We obtained optical data for morphological analysis using the software package GALFIT and have identified AGN by their X-ray properties. We analyzed the morphological properties of the groups individually and analyzed the AGN fractions of binned groups and clusters corresponding to different velocity dispersions and thus number density environments. This analysis is not conclusive but suggests that the group environment may be the ideal environment for the triggering and fueling of low-luminosity X-ray identified AGN.

We developed a method to quantitatively analyze galaxy morphologies using GALFIT in order to conduct morphological studies of galaxies in our sample. Our data suggest that the X-ray AGN fraction decreases among clusters with higher velocity dispersions. We compare our results to a value of the X-ray identified AGN fraction among early-type galaxies for the field (B. Lehmer 2006, private communication) and note that this fraction is smallest in the highest velocity dispersion clusters in our sample ($4.4^{+2.2}_{-1.5}$%), rises in the group environments to $12.0^{+5.5}_{-3.9}$%, and is again smaller in the field, at $6.6^{+3.4}_{-2.4}$% (B. Lehmer 2006, private communication). We find that the low velocity dispersion groups have an AGN fraction that is larger than the high velocity dispersion clusters. We interpret this difference as a result of the interaction based model of low-luminosity AGN fueling: available cold gas and gravitational interactions activate and fuel AGN. The cluster environment, while dense enough to encourage interactions (though, with higher velocity dispersions to discourage bound pairs and mergers), may lack the cold gas necessary for AGN fueling. The field galaxies, though rich in cold gas, are too isolated for a significant number of interactions to occur. The group environment, with its moderate number density and available cold gas, seems to encourage the production of X-ray AGN that we are sensitive to discovering. From this observation, we conclude that the morphological mix of galaxies is not the sole contributor to the different AGN fractions in different number density environments.

REFERENCES

Adelman-McCarthy, J. K., et al. 2008, ApJS, 175, 297

Adelman-McCarthy, J. K., et al. 2006, ApJS, 162, 38

Baldwin, J. A., Phillips, M. M., & Terlevich, R. 1981, PASP, 93, 5

Balogh, M. L., Navarrow, J. F., & Morris, S. L. 2000, ApJ, 540, 113

Begelman, M. C. 2004, in Ho L. C., ed., Coevolution of Black Holes and Galaxies. Cambridge Univ. Press, Cambridge, p. 374

Bell, E. F., et al. 2004a, ApJ, 600, L11

Bernardi, M., Sheth, R K., Nichol, R. C., Schneider, D. P., & Brinkmann, J., 2005, AJ, 129, 61

Bertin, E., & Arnouts, S. 1996, A&AS, 117, 393

Byrd, G., & Valtonen, M. 1990, ApJ, 350, 89

Conselice, C. J., Bershady, M. A., & Jangren, A. 2000, ApJ, 529, 886

Cowie, L. L., & Songaila, A. 1977, Nature, 266, 501

Di Matteo, T., Springel, V., & Hernquist, L. 2005, Nature, 433, 604

Dressler, A. 1980, ApJ, 236, 351

Dressler, A., Thompson, I. B., & Shectman, S. A., 1985, ApJ, 288, 481

Eke, V. R., et al. 2004, MNRAS, 348, 866

Ferrarese, L., & Merritt, D. 2000, ApJ, 539, L9

Gebhardt, K., et al. 2000, ApJ, 539, L13

Gehrels, N. 1986, ApJ, 303, 336

Gehrens, T., Fried, J., Wehinger, P. A., & Wyckoff, S. 1984, ApJ, 278, 11

Giovanelli, R., & Haynes, M. P. 1985, ApJ, 292, 404

Goto, T., et al. 2003, MNRAS, 346, 601

Grogin, N. A., et al. 2005, ApJ, 627, 97

Gunn, J. E., & Gott, J. R. I. 1972, ApJ, 176, 1

Haeussler, B., et al. 2007, ApJS, 172, 615

Ho, L. C., Filippenko, A. V., & Sargent, W. L. 1997, ApJ, 487, 568

Hopkins, P. F., et al. 2005, ApJ, 630, 705

Hutchings, J. B., Crampton, D., & Campbell, B. 1984, ApJ, 280, 41

Kauffmann, G., et al. 2003, MNRAS, 346, 1055

Kauffmann, G., et al. 2004, MNRAS, 353, 713

Kewley, L., Dopita, M., Sutherland, R., Heisler, C., Trevena, J., 2001, ApJ, 556, 121

Larson, R.B., Tinsley, B.M., & Caldwell, C.N. 1980, ApJ, 237, 692

Lintott, C. J., et al. 2008, MNRAS, 389, 1179

Lynden-Bell, D., 1969, Nat, 223, 690

Malkan, M. A., Margon, B., & Chanan, G. A. 1984, ApJ, 280, 66

Martini, P., Kelson, D. D., Kim, E., Mulchaey, J. S., & Athey, A. A. 2006, ApJ, 644, 116

Martini, P., Mulchaey, J. S., & Kelson, D. D. 2006, ApJ, 644, 116

Merchán, M., & Zandivarez, A. 2002, MNRAS, 335, 216

McGee, S. L., et al. 2008, MNRAS, 387, 1605

McIntosh, D. H., et al. 2005, ApJ, 632, 191

Merritt, D. 1984, ApJ, 276, 26

Miller, R. H. 1986, a, 167, 41

Miller, C. J., et al. 2003, ApJ, 597, 142

Mulchaey, J. S., et al. 2009, in preparation

Peng, C. Y., Ho, L. C., Impey, C. D., & Rix, H. 2002, ApJ, 124, 266

Popesso, P., & Biviano, A. 2006, A&A, 460, L23

Quilis, V., Moore, B., & Bower, R. 2000, Science, 288, 1617

Rasmussen, J., et al. 2006, MNRAS, 373, 653

Richstone, D. O. 1976, ApJ, 204, 642

Sérsic, J. L. 1968, Atlas de Galaxias Australes (Cordoba: Obs. Astron.)

Shen, Y., et al. 2006, ApJ, 654, L115

Shimada, M., et al. 2000, AJ, 119, 2664

Silverman, J. .D., et al. 2008, ApJ, 675, 1025

Simard, L. 2002, ApJS, 142, 1

Sivakoff, G. R., Martini, P., Zabludoff, A. I., Kelson, D. D., & Mulchaey, J. S. 2008, ApJ, 682, 803

Smith, E., et al. 1986, ApJ, 306, 64

Spitzer, L. J., & Baade, W. 1951, ApJ, 113, 413

Springel, V., Di Matteo, T., & Hernquist, L. 2005, ApJ, 620, L79

White, S. D. M. 1978, MNRAS, 184, 185

de Vaucouleurs, G. 1948, Ann. d'Astrophys. 11, 247